Reactive iron as an important reservoir of marine organic carbon over geological timescales

Yunru Chen[1], Liang Dong[2], Weikang Sui[2], Mingyang Niu[1], Xingqian Cui[2], Kai-Uwe Hinrichs[4], Fengping Wang[1,2,3*]

1. State Key Laboratory of Microbial Metabolism, School of Life Sciences and Biotechnology, Shanghai Jiao Tong University, Shanghai 200240, China

2. School of Oceanography, Shanghai Jiao Tong University, Shanghai 200240, China

3. Southern Marine Science and Engineering Guangdong Laboratory (Zhuhai), Zhuhai 519000, China

4. MARUM-Center for Marine Environmental Sciences and Department of Geosciences, University of Bremen, D-28359 Bremen, Germany

*Correspondence: fengpingw@sjtu.edu.cn

1   Reactive iron (Fe_R) has been suggested to serve as a semi-persistent sink of organic

2   carbon (OC) in surface marine sediments, where approximately 10-20% of total OC

3   (TOC) is associated with Fe_R (Fe_R-OC). However, the persistence of Fe_R-OC on

4   geological timescales remains poorly constrained. Here, we retrieved Fe_R-OC records

5   in two long sediment cores of the northern South China Sea spanning almost the past

6   100 kyrs. Most prominently, the downcore marine-sourced Fe_R-OC contributes a

7   relatively stable proportion of 13.3±3.2% to TOC. However, distinctly lower values of

8   less than 5% of TOC, accompanied by notable ^{13}C depletion of Fe_R-OC are observed

9   in the sulfate-methane transition zone (SMTZ), where active sulfate reduction and

10   potential iron reduction are indicated by microbial composition and geochemical

11   modelling. Fe_R-OC is suggested to be remobilized by microbially mediated reductive

12   dissolution of Fe_R (and might be substituted with freshly formed ^{13}C-depleted OC).

13   The global budget of Fe_R-OC in microbially active Quaternary marine sediments

14   could be as large as $219 \pm 133 \times 10^{17}$ g, which is 18-48 times the size of the atmospheric

15   carbon pool. Thus, sedimentary Fe_R-OC as an exchangeable reservoir of labile OC

16   may support deep life and play a role in regulating Earth's carbon cycle over

17   geological timescales.

Introduction

Reactive iron (Fe$_R$, defined as iron (oxyhydr)oxides that can be reductively dissolved by sodium dithionite) can promote the preservation of organic carbon (OC) in a wide range of terrestrial and marine environments[1-5], as OC associated with Fe$_R$ (Fe$_R$-OC) has long been believed to be more resistant to microbial degradation under aerobic conditions[6, 7]. A proportion of ~21.5±8.6% of the OC in surface marine sediments was estimated to be directly associated with Fe$_R$, which corresponds to a global mass of 19-45×10^{15} grams of OC[1] (roughly 2-5% of the amount of the atmospheric CO_2). This proportion was reassessed to 15.6±6.5% after incorporating more estuarine sediment samples[8], nevertheless demonstrating its great potential and significant role in preserving the sedimentary OC.

Besides protecting OC from degradation, Fe$_R$ also acts as active electron acceptor for anaerobic microbial respiration[9, 10]. Its reduction could potentially weaken or even break the association between Fe$_R$ and OC. Indeed, recent studies demonstrated that Fe$_R$-OC can be remobilized during microbial iron reduction and subsequently utilized as electron donor and/or carbon source for microbial communities[11-14]. However, the evaluation on the fate of Fe$_R$-OC in marine sediments were mostly based on less than 0.5-m-long sediment cores, covering less than ten thousand years in age[15, 16]. A gradual decline in the Fe$_R$-OC percentage in total OC (TOC) on the centennial to millennial scale has been observed, suggesting the instability of Fe$_R$-OC[15]. Sun et al. (2020) reconstructed the Fe$_R$-OC record of a sediment core in the Yangtze River

Estuary, which showed potential persistent of Fe_R-OC for the past 55 kyrs[17]. However, in this study age of the core bottom was calculated from the core length and estimated sedimentation rate, and there was no further data measured to explain the variation of Fe_R-OC in the core. Nevertheless, little is known about the behaviour of Fe_R-OC on longer timescales, especially with respect to the impact of diagenetic processes such as microbial degradation.

On geological timescales, the burial rate of sedimentary OC exerts major control on the concentrations of atmospheric O_2 and CO_2[18] and thus substantially influences Earth's environmental conditions. As a significant proportion of sedimentary OC, the balance of preservation and remobilization of Fe_R-OC is thus of great importance for both the carbon cycle and its potential contribution for fueling subsurface microbial communities.

Here, two distinct gravity cores (QDN-G1 and QDN-14B, Fig. 1a) of the northern South China Sea were chosen in order to determine the fate of the sedimentary Fe_R-OC via its quantitative and isotopic analysis. The core QDN-G1 represents typical continental slope sediments (1478 m water depth), while core QDN-14B (1370 m water depth), around 35 km southwest away from the core QDN-G1, was influenced by nearby cold seeps expelling methane-rich fluids[19]. Consequently, QDN-14B can be used to comparatively evaluate the influence of microbial activities on the potential remobilization of Fe_R-OC in the diagenetically active zones where sulfate reduction

coupled to either organic matter remineralization or methane oxidation occurs.

Meanwhile, the core QDN-G1 with relatively low microbial activity is used for

exploring the long-term preservation of Fe_R-OC on glacial/interglacial timescales.

To quantify the amount of Fe_R-OC, the citrate-bicarbonate-dithionite (CBD) method

described in detail by Lalonde et al.[1] and Salvadó et al.[2] was applied in this study (see

Methods). This method targets only reactive iron (oxyhydr)oxides, which are

presumably accessible for microorganisms, and leaves unreactive phases such as iron-

containing silicates untouched[20]. By incorporating analyses of pore water

geochemistry, including the concentrations of sulfate, ferrous iron, dissolved inorganic

carbon (DIC), and the carbon isotope ratio of DIC ($\delta^{13}C_{DIC}$), all of which are tied to

microbially mediated processes, our study takes a critical step in assessing the

stability of sedimentary Fe_R-OC in response to post-depositional microbial activities

and sheds lights on its persistence and remobilization on geological timescales.
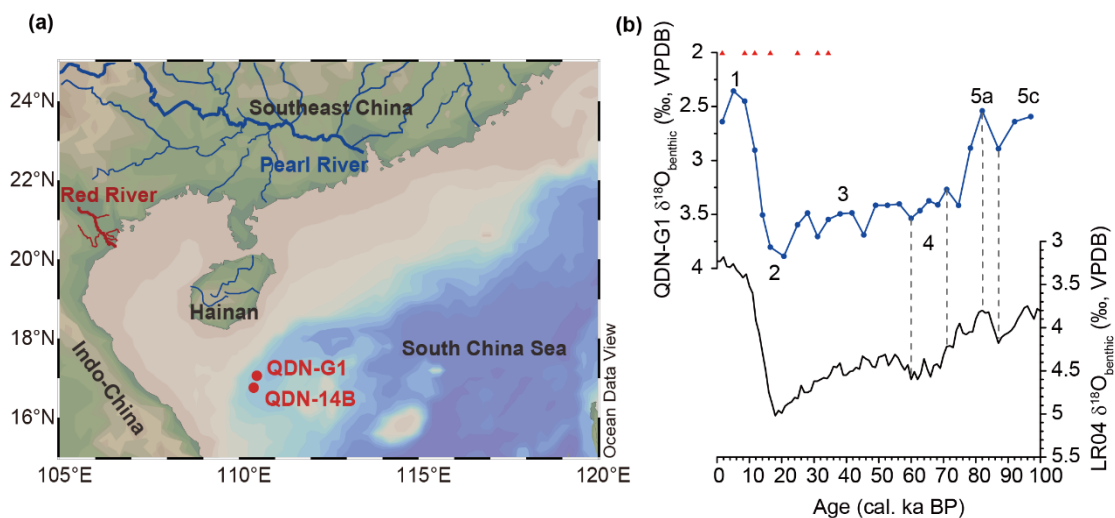
Fig. 1. Map of the cores studied in the northern South China Sea and age model of core

5

QDN-G1. (a) Map of cores QDN-G1 and QDN-14B. River systems entering the northern South

China Sea are indicated by blue and red lines. (b) Age model of core QDN-G1. The age model of

the upper 4.0 m (0-34.4 ka) was based on 7 accelerator mass spectrometry ^{14}C ages of planktonic

foraminifera (*G. ruber*) (red triangles). The age model of the lower 6.8 m (34.4-97.0 ka) was

established by aligning the δ^{18}O record of benthic foraminifera (*C.wuellerstorfi*) (blue line) to the

global benthic δ^{18}O stack LR04[21] (black line). The tie points used for the alignment are indicated

by dashed grey lines (see Methods for detailed information).

Result and discussion

Content and biogeochemistry of Fe$_R$-OC in long-buried sediments

The core recovery of QDN-G1 and QDN-14B were 10.8 m and 8.4 m, respectively.

These two cores penetrated vastly different benthic ecosystems. Microbially mediated

early diagenetic redox reactions have resulted in a distinct geochemical zonation, i.e.,

the iron reduction zone (IRZ), the sulfate reduction zone (SRZ), the sulfate-methane

transition zone (SMTZ), and the methanogenic zone (MZ) (Fig. S1 and S2). Despite

similar TOC content in sediments from the two cores (Fig. 2b and g, black lines), the

higher methane fluxes and the associated rapid depletion of sulfate via anaerobic

oxidation of methane resulted in a shallower SMTZ in core QDN-14B (280-440

cmbsf) compared to core QDN-G1 (potentially around 720-960 cmbsf) (Fig. S1 and

S2). This is backed up by geochemical modelling results (see Methods), which

showed a more than two times higher net sulfate reduction rate in the SMTZ in core

QDN-14B compared to core QDN-G1 (0.034 vs. 0.015 mol m^{-3} yr^{-1}) (Fig. S3).

101

TOC content in the two cores ranges from 0.4 to 1.2%, except for low content in a

coarsely grained layer (410-420 cmbsf in QDN-14B[22]) (Fig. 2b and g, black lines).

The Fe_R-OC content ranges from 0.04 to 0.17% (Fig. 2b and g, red lines) and accounts

for 10-20% of TOC (Fig. 2d and i). However, interestingly, both the lowest Fe_R-OC

content and the lowest Fe_R-OC/TOC values occurred in the SMTZ of each core. In

QDN-G1 and QDN-14B, the average content of Fe_R-OC in non-SMTZ sediments are

0.12% and 0.10%, respectively, but drop to 0.06% and 0.03% in the SMTZ sediments,

respectively (Table 1). Similarly, the average Fe_R-OC/TOC values in the non-SMTZ

layers are 14.0% and 13.0%, but drop to 12.3% and 5.2% in the SMTZ sediments,

respectively (Table 1).

112

The carbon isotope ratios of TOC ($\delta^{13}C_{TOC}$) and Fe_R-OC ($\delta^{13}C_{FeR-OC}$) provide insights

into the sources of the corresponding OC pool. In the two cores, $\delta^{13}C_{TOC}$ varies

mostly between $-22.5‰$ and $-19.7‰$ (Figure 2c and h, black lines), indicating the

accumulation of mainly marine-algal OC, which in the sampled area has an average

$\delta^{13}C$ value of $-20.8\pm0.4‰$[23]. $\delta^{13}C_{FeR-OC}$ is generally similar with $\delta^{13}C_{TOC}$ (Figure 2c

and h, red lines), suggesting that Fe_R are mainly associated with marine-sourced OC

as well. However, somewhat lower $\delta^{13}C_{TOC}$ and $\delta^{13}C_{FeR-OC}$ values in SMTZ sediments

are observed in both cores (Figure 2c and h). The average $\delta^{13}C_{TOC}$ values of SMTZ

sediments are 1.5‰ and 1.9‰ lower than those of non-SMTZ sediments in QDN-G1

and QDN-14B, respectively (Table 1). Similarly, the average $\delta^{13}C_{FeR-OC}$ values of

7

123   SMTZ sediments are 3.1‰ and 2.8‰ lower than those of non-SMTZ sediments in

124   QDN-G1 and QDN-14B, respectively (Table 1).

125

126   Taken together, lower Fe_R-OC content, lower Fe_R-OC/TOC values, along with more

127   depleted $\delta^{13}C_{FeR\text{-}OC}$ are observed in SMTZ sediments, comparing to uniform records

128   in non-SMTZ sediments. The conspicuous characteristics in the SMTZ could result

129   from either processes before deposition such as coincidental changes in sediment

130   provenance, OC input and burial efficiency, and/or post-depositional processes related

131   to sedimentary microbial activity. The age model of core QDN-G1 shows that it

132   covers a complete glacial-interglacial cycle since MIS5c (Fig. 1b), and no clear

133   glacial-interglacial pattern of TOC and Fe_R-OC records is evident (Fig. 2 and Fig. S4)

134   (see Supplementary Text for details). Assuming similar sedimentation rates in core

135   QDN-14B, the variations in TOC and Fe_R-OC records do not follow the glacial-

136   interglacial cycles either. Combining especially low Fe_R-OC content and depleted

137      $\delta^{13}C_{FeR\text{-}OC}$ in the SMTZ, which is usually a horizon of high microbial activity, we

138   propose that the post-depositional microbial processes account for these distinctive

139   characteristics of Fe_R-OC records.
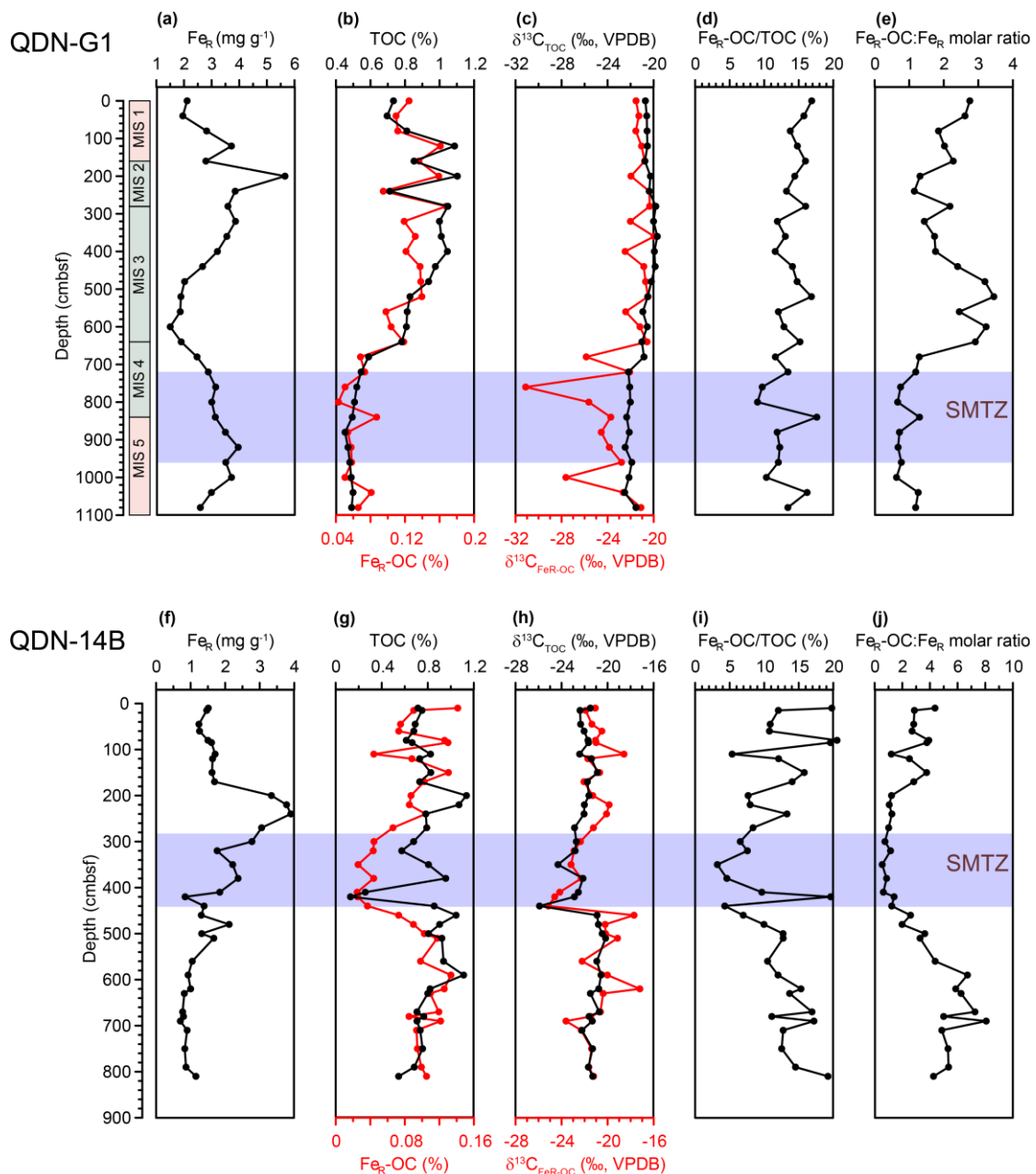
Fig. 2. **Content and $\delta^{13}C$ profiles of TOC and Fe_R-OC in cores QDN-G1(a-e) and QDN-14B**

(f-j). The marine isotope stages (MIS) assigned based on the age model are plotted against the

depth axes for core QDN-G1. The pink and green bars indicate interglacial periods and the last

glacial period, respectively. (a and f) Content of Fe_R. (b and g) Content of TOC (black lines) and

Fe_R-OC (red lines). Separate x-axes are used for TOC and Fe_R-OC, respectively, labelled in the

same color as the data profile. (c and h) Carbon isotope ratios of TOC (black lines) and Fe_R-OC

(red lines). Separate x-axes are used for TOC and Fe_R-OC, respectively, labelled in the same color

9

148   as the data profile. (d and i) Percentage of Fe_R-OC in TOC. (e and j) The molar ratio of Fe_R-OC

149   and Fe_R. The locations of the SMTZ are highlighted by the purple bars.

150

151   Table 1 Comparisons of the content and carbon isotope ratios of TOC and Fe_R-OC between non-

152   SMTZ and SMTZ sediments in two cores.

QDN-G1					
	TOC (%)	Fe_R-OC (%)	Fe_R-OC/TOC (%)	$\delta^{13}C_{TOC}$ (‰, VPDB)	$\delta^{13}C_{FeR-OC}$ (‰, VPDB)
Non-SMTZ[a] (N = 21)	0.8±0.2	0.12±0.03	14.0±1.9	-20.6±0.7	-21.8±1.8
SMTZ[a] (N =7)	0.5±0.0	0.06±0.01	12.3±2.8	-22.2±0.2	-24.8±3.0
Offset between non-SMTZ and SMTZ sediments[b]	0.3	0.06	1.8	1.5	3.1
QDN-14B					
	TOC (%)	Fe_R-OC (%)	Fe_R-OC/TOC[c] (%)	$\delta^{13}C_{TOC}$ (‰, VPDB)	$\delta^{13}C_{FeR-OC}$ (‰, VPDB)
Non-SMTZ[a] (N = 29)	0.8±0.1	0.10±0.02	13.0±4.0	-21.5±0.7	-20.8±1.4
SMTZ[a] (N = 7)	0.6±0.3	0.03±0.01	5.2±1.8[c]	-23.3±1.3	-23.5±1.1
Offset between non-SMTZ and SMTZ sediments[b]	0.2	0.07	7.7	1.9	2.8

153   [a]Given are means±standard deviation.
154   [b]Offsets of corresponding averaged values between non-SMTZ and SMTZ sediments.
155   [c]Fe_R-OC/TOC data at 410 and 420 cmbsf in QDN-14B are biased by extremely low TOC and are
156   not included for calculations (N = 5).

157

158   **Fe_R-OC remineralization coupled to microbial processes in the SMTZ**

159   The SMTZ, as a discrete sedimentary horizon where anaerobic oxidation of methane

160   is coupled to sulfate reduction (S-AOM)[24], ubiquitously occurs in organic-rich marine

161   shelf and slope sediments. S-AOM is performed syntrophically by sulfate-reducing

162   bacteria and methanotrophic archaea[25]. In core QDN-14B, geochemical modelling

163   reveals higher net sulfate reduction rates in the SMTZ (Fig. 3b), which is further

164   supported by (1) the higher relative abundance and cell concentration of sulfate-

165 reducing bacteria (Fig. 3e and f), and (2) elevated copy number of methyl-coenzyme

166 M reductase subunit A (*mcrA*) gene (Fig. 3g)[19], the key marker gene for methane

167 metabolism by archaea including S-AOM as the main process consuming sulfate in

168 the SMTZ[26]. By contrast, in core QDN-G1, there is no evidence for elevated sulfate

169 reduction activity in the SMTZ compared to the shallower sulfate reduction zone,

170 based on modelled rates and both relative abundance and cell number of sulfate-

171 reducing bacteria (Fig. S5b, e and f). This is consistent with the relatively moderate

172 variation in Fe_R-OC/TOC record in core QDN-G1 compared to that in core QDN-

173 14B. Collectively, these lines of evidence suggest that due to the particularly high

174 methane flux at core QDN-14B, the microbial activity in the SMTZ has stimulated the

175 remobilization of Fe_R-OC.

176

177 A plausible mechanism for lower Fe_R-OC content in the SMTZ is the occurrence of

178 reductive dissolution of Fe_R by the hydrogen sulfide produced during sulfate

179 reduction[27, 28], and subsequent remobilization of Fe_R-OC. Apart from chemical

180 reduction of Fe_R, sulfate-reducing bacteria may also reduce Fe_R directly[29], with the

181 rate of reduction being enhanced by sulfate reduction and the presence of biogenic

182 sulfide[30]. In addition, the process of AOM may be directly coupled with iron reduction

183 (Fe-AOM)[31] and facilitate Fe_R dissolution in this zone. In sum, the reduction of Fe_R

184 could be enhanced by biological and chemical processes in the SMTZ, and result in

185 the remobilization of Fe_R-OC.

186

187   The observed negative inflections of $\delta^{13}C_{FeR-OC}$ in the SMTZ of the two cores can be

188   mainly caused by the re-adsorption of ^{13}C-depleted dissolved organic carbon (DOC)

189   in the pore waters produced in two ways. First, remobilized Fe_R-OC is released into

190   the pore water as DOC and seletively remineralized by microorganisms, which

191   preferentially degrade ^{13}C-enriched labile DOC (e.g., carbohydrates and proteins)[32]

192   and leave behind ^{13}C-depleted DOC. Second, ^{13}C-depleted DOC can be produced

193   during AOM in the SMTZ[33]. The adsorption of DOC molecules depends on the

194   availability of binding sites on Fe_R mineral surface. The molar ratio of Fe_R-OC and

195   Fe_R has been interpreted as an indicator of the binding mechanism between Fe_R and

196   OC, with monolayer adsorption resulting in a molar ratio lower than 1 while

197   coprecipitation leads to higher ratios of 6-10[34, 35]. The molar ratios of Fe_R-OC to Fe_R

198   in both SMTZs are below 1, indicating abundant binding sites available for DOC

199   molecules (Fig. 2e and j). Isotopically depleted DOC in the pore waters of SMTZ

200   sediments can therefore be re-adsorbed on the surface of Fe_R and result in negative

201   $\delta^{13}C_{FeR-OC}$ values.

202
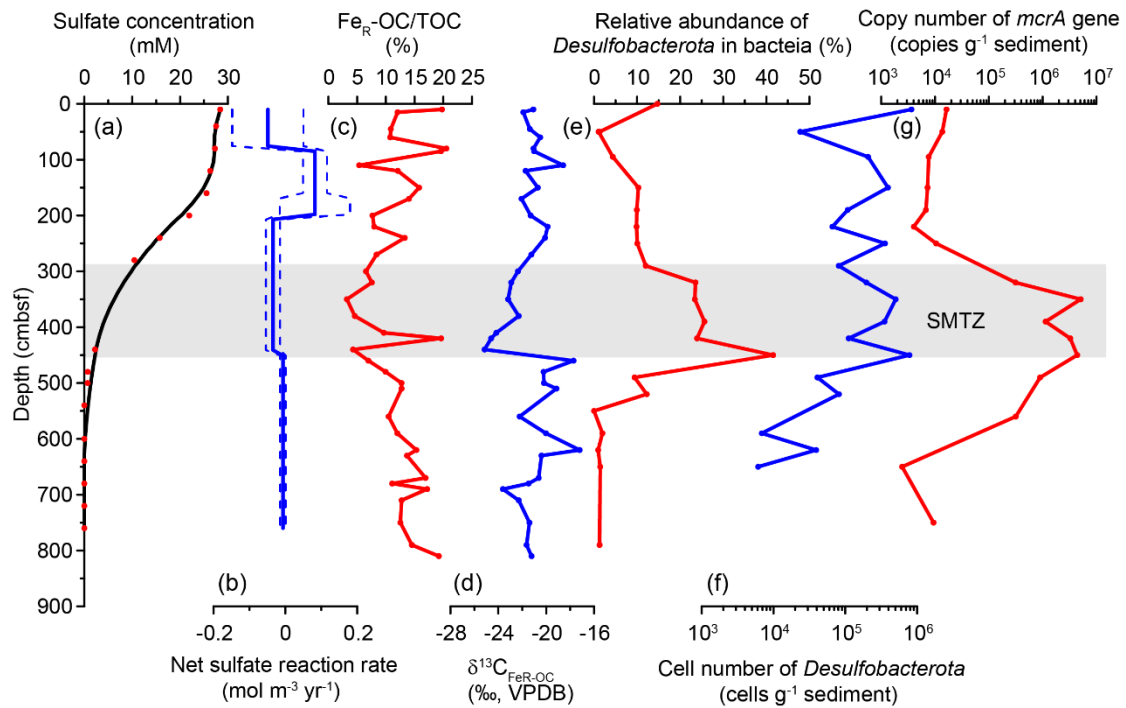
Fig. 3. Geochemical modelling and microbial evidence show that a high sulfate reduction rate is associated with low Fe$_R$-OC/TOC ratios in the SMTZ of QDN-14B. (a) Measured (red dots) and fitted (black line) sulfate concentrations. A 5-point Gaussian filter was applied to the concentration with the weighting on the 5 points of: [0.06, 0.24, 0.4, 0.24, 0.06][36]. (b) Modelled net reaction rate profile of sulfate. Negative values indicate net consumption, and positive values indicate net production. The 1σ envelope is shown in dashed line (See Methods for details). (c) Downcore record of Fe$_R$-OC/TOC. (d) Down-core record of δ^{13}C$_{FeR-OC}$. (e) Relative abundance of *Desulfobacterota* in bacteria, to which most of the sulfate-reducing bacteria belong to[37]. (f) The cell number of *Desulfobacterota*, translated from the cell number of bacteria by multiplying the relative abundance of *Desulfobacterota* in bacteria. (g) The copy number of *mcrA* gene (data from Niu et al., 2017[19]). The grey bar shows the position of SMTZ.

Remineralization of Fe$_R$-OC supports microbial communities in the SMTZ

In the two cores studied, the depth interval of SMTZ in core QDN-14B is well defined

218   with the depletion of sulfate, increasing DIC, and depleted $\delta^{13}C_{DIC}$ (Fig. S2).

219   Therefore, core QDN-14B is used to estimate the remineralization of TOC and Fe_R-

220   OC in the SMTZ. The accumulation rate of TOC and Fe_R-OC are calculated by

221   multiplying their content in sediments by the sediment mass accumulation rate (see

222   Methods). Assuming that all the TOC and Fe_R-OC lost in the SMTZ is remineralized

223   by heterotrophic microorganisms, the remineralization flux of TOC and Fe_R-OC in the

224   SMTZ can be estimated as the difference of their mean accumulation rate between the

225   sediment column above and within the SMTZ. This way, the TOC and Fe_R-OC

226   remineralization fluxes are estimated to be 15.8 and 5.8 mol m^{-2} kyr^{-1} in the SMTZ of

227   QDN-14B, respectively. Fe_R-OC remineralization contributes 36.7% of the TOC

228   remineralization in QDN-14B. As the percentage of Fe_R-OC in TOC is 10-20% in

229   core QDN-14B, Fe_R-OC is preferentially remineralized compared to non-Fe_R-OC in

230   the SMTZ of QDN-14B. Therefore, stimulated by more active microbial processes,

231   e.g., S-AOM, Fe-AOM, and iron reduction, Fe_R-OC is remobilized and potentially

232   remineralized in the SMTZ. This may contribute a substantial part to OC

233   remineralization in the SMTZ. Moreover, since Fe_R-OC is likely enriched in labile

234   organic matter[1], it has the potential to enhance heterotrophic microbial communities

235   in subsurface sediments and be rapidly recycled upon remobilization.

236

237   The magnitude of the Fe_R-OC remineralization flux estimated in the SMTZ in core

238   QDN-14B is supported by a similar flux in core QDN-G1 (5.0 mol m^{-2} kyr^{-1}); the

239   latter flux was estimated in the same way with the limitation of the SMTZ interval

being constrained with more uncertainty. Considering that the SMTZ is ubiquitous in

continental slope sediments[26], and assuming an Fe_R-OC remineralization flux of 5.8

mol m^{-2} kyr^{-1} in the SMTZ and a continental slope area of 3.01×10^7 km^2 [26], the

global Fe_R-OC remineralization flux in the SMTZ of the continental slope area is

estimated to be 0.17 Tmol yr^{-1}, which is about one third of the methane consumption

flux in the SMTZ of continental slope sediments (0.56 Tmol yr^{-1} [26]) and 1% of the

global sedimentary OC burial rate (13.3 Tmol yr^{-1} [38]). Using acetate as a proxy for

OC, and the Gibbs energies of OC oxidation by sulfate of -81.5 KJ (per mol acetate)[39]

at 5°C and 100 bars of pressure (1000 m water depth), the remineralization of Fe_R-OC

in the SMTZ of the continental slope can provide a power supply of 6.9×10^{15} J yr^{-1}.

Assuming the cellular power demand for organisms oxidizing OC with sulfate of

7.7×10^{-14} W cell^{-1} [39], the Fe_R-OC remineralization in the SMTZ of continental slope

area could sustain a biomass of 2.8×10^{21} cells. Considering generally lower power

demand of 10^{-20} to 10^{-16} W cell^{-1} for microorganisms in marine subsurface sediments,

this amount of energy could potentially support an even larger population of 10^{24} to

10^{28} cells. Given the estimated global microbial cell quota of 2.9×10^{29} in marine

sediments [40], the remineralization of Fe_R-OC could support a substantial fraction of

subseafloor microbial life.

Reactive iron as an important reservoir of labile OC over geological timescales in

marine sediments

The binding mechanism between Fe_R and OC in marine sediments has been inferred

262 from the molar ratio of Fe_R-OC to Fe_R[1], with adsorption and coprecipitation

263 characterized by ratios of <1 and 6-10, respectively[1, 35]. In the two cores studied here,

264 the molar ratio of Fe_R-OC to Fe_R is always larger than 1, except in the SMTZ,

265 suggestive of a mixed binding mechanism of adsorption and coprecipitation (Fig. 2e

266 and j). In marine sediments, Fe_R can be reductively dissolved under anaerobic

267 conditions developed during early diagenesis[10]. The upward diffusing Fe^{2+} can

268 coprecipitate with marine OC into authigenic Fe_R after oxidation at the redox

269 interface[41]. Previous work in Arctic shelf sediments suggested that authigenic

270 coprecipitation is not the dominant binding mechanism of OC and Fe_R[15]. In our study,

271 $\delta^{13}C_{FeR-OC}$ in both sediment cores are typical for marine-sourced OC and the high

272 molar ratio of Fe_R-OC to Fe_R indicates coprecipitation as an important binding

273 mechanism. We propose that a large proportion of Fe_R-OC is formed at the redox

274 interface in marine environments, which could be formed either autochthonously after

275 deposition, or allochthonouly in neighbouring surface sediments and transported to

276 the core location as resuspended particulates[42, 43].

277

278 The global budget of Fe_R-OC has been estimated to be $19\text{-}45\times10^{15}$ g C in surficial

279 marine sediments[1], roughly 2-5% of the amount of the atmospheric CO_2 (875×10^{15} g

280 C[44]). However, the estimation of the Fe_R-OC budget in long-buried sediments is

281 hindered by the uncertain fate of Fe_R-OC after deposition during early diagenesis. Our

282 results can fill this gap and advance the estimation of global Fe_R-OC budget in

283 subsurface sediments. The average Fe_R-OC/TOC ratio in the two cores studied, except

16

within the SMTZ in QDN-14B, is 13.3±3.2%. As revealed by the records of QDN-14B, the percentage of Fe_R-OC in TOC is much lower in SMTZ sediments, where iron reduction is enhanced significantly by processes likely induced by sulfate reducing bacteria, methanotrophic archaea and/or biogenic sulfide. This leads to especially low Fe_R-OC/TOC in certain geochemical horizons with high microbial activities, e.g., SMTZ. A cryptic sulfur cycle driven by Fe_R has been recently proposed to take place in methanic sediments [45, 46], where sulfate is generated from the re-oxidation of sulfide by Fe_R and sustain sulfate reduction. This may also cause the reductive dissolution of Fe_R and remobilize Fe_R-OC. However, low Fe_R-OC/TOC values were not observed in the methanogenic zone of both QDN-14B and QDN-G1, which may be due to the low sulfate reduction rates in this zone[45]. Furthermore, the records of QDN-G1 demonstrate that the percentage of Fe_R-OC in TOC remains relatively stable for almost 100 ka. The Fe_R-OC records in these two cores suggest that a stable proportion of TOC survives early diagenesis as Fe_R-OC and is sequestered in marine sediments over glacial/interglacial cycles, which facilitate the estimation of global Fe_R-OC budget in long-buried sediments by multiplying the corresponding TOC budget and Fe_R-OC/TOC ratios in surface marine sediments. LaRowe et al. (2020)[39] estimated the TOC budget in marine sediments throughout the Quaternary Period (0-2.59 Ma), which includes the most microbially active sediments. Therefore, the budget of Fe_R-OC in Quaternary marine sediments, regarded as exchangeable under the influence of microbial processes, can be estimated.

As the study on the fate of Fe_R-OC in long buried sediments is still in its infancy and the supporting data are lacking, our estimation makes the following assumptions: First, the Fe_R-OC/TOC ratio remains relatively stable in Quaternary sediments. Although our records spanning the past around 100 kyrs strongly support this assumption, it is suggested that the degradation rate of Fe_R-OC is slower than non-Fe_R-OC[6, 7, 16]. Therefore, an increasing percentage of Fe_R-OC in TOC is expected in long-buried sediments, which could lead to a higher global Fe_R-OC budget than our estimation. Second, our study gives the first record of Fe_R-OC behavior during early diagenesis in continental shelf sediments. The fate of Fe_R-OC in other depositional setting remains unknown. We assume that the Fe_R-OC/TOC ratio in long buried sediments also stays relatively stable in other depositional settings. Third, there is only limited data available from abyssal sediments (water depth >3500 m), the Fe_R-OC/TOC ratio in the surface sediments of marginal sediments (200m < water depth<3500m) is used to represent both marginal and abyssal environments. In spite of these caveats, our estimation provides a premilinary but straightforward view of how much OC has beensequestered by reactive iron phases and serve as a semi-stable carbon pool over geological timescales.

To estimate the global budget of Fe_R-OC in Quaternary sediments, all the published Fe_R-OC/TOC data in marine sediments using the CBD method are compiled with our measured data and grouped into four categories based on their study area information: deltaic and estuarine sediments, continental shelf sediments, continental slope and

deep-sea sediments, and sediments in anoxic/sulfidic regions (Table S3). The mean

values of Fe_R-OC/TOC are 15.7±7.8%, 11.2±3.7%, 20.1±9.3% and 22.9±4.8%,

respectively (Figure 4). A one-way ANOVA was used to determine whether the Fe_R-

OC/TOC values are significantly different among these mairne environments. The

results show that Fe_R-OC/TOC values significantly differ between anoxic/sulfidic

sediments and continental shelf sediments ($P<0.001$) and between continental slope

and deep-sea sediments and continental shelf sediments ($P<0.05$) (Figure 4).

Considering the limited distribution and limited published data of the anoxic/sulfidic

regions, this category is not further considered in the global estimation. Delta/estuary

and continental shelf are combined, representing the marine environment with water

depth shallower than 200 m. The Fe_R-OC/TOC ratios of all the study areas belonging

to this environment are averaged to be 13.2±6.1% (Table S4). The continental slope

and deep sea represent the marine environment with water depth deeper than 200 m,

where the Fe_R-OC/TOC ratios of all the study areas belonging to this environment

average at 20.1±9.3% (Table S4). Combining the published TOC storage of these two

environments in Quaternary sediments [39], the global budget of Fe_R-OC in Quaternary

marine sediments was estimated to be $291±133×10^{17}$ g C (Table S4), which is

approximately 18-48 times the size of the atmospheric carbon pool.

Our results suggest Fe_R-OC as a persistent but exchangeable pool of labile OC that

potentially plays a critical role in modulating Earth's climate over geological

timescales. This large preserved carbon pool can be especially remobilized in

350 microbial active zones like SMTZ. Given the context that the location of SMTZ can

351 migrate upward and downward in response to sedimentation deposition with varied

352 OC flux over glacial/interglacial timescales[47], Fe_R-OC in different sedimentary layers

353 might be consequently remobilized and fuel up the surrounding microbial community.

354 This would also bring uncertainties to the balance of OC preservation and degradation

355 in long-buried sediments. Therefore, further researches are required to fully

356 understand the role of reactive iron phases in long-term carbon sequestration in

357 marine environments.

358
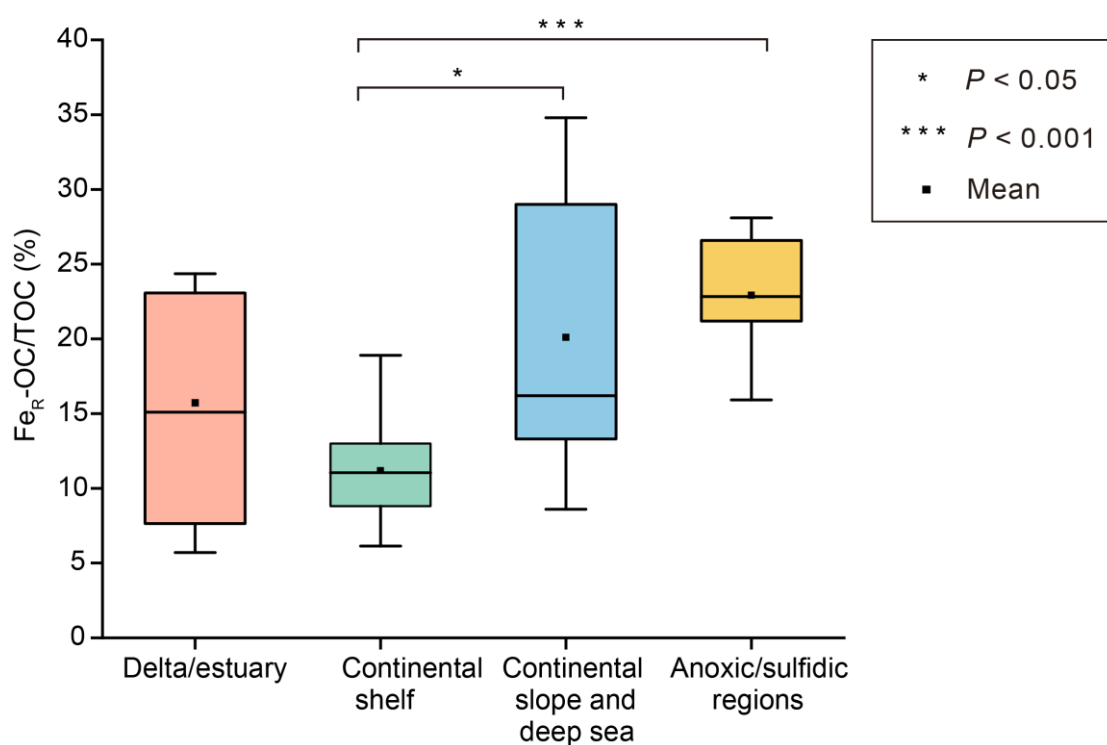
359

360 **Fig. 4. Fe_R-OC/TOC values in different marine environments.** All the published Fe_R-OC/TOC

361 data obtained from marine sediments using the CBD method are compiled (detailed information of

362 study areas and references are listed in Table S3). The Fe_R-OC/TOC value of each study area is

363 represented by the mean value of all data collected from this study area in the same study case to

364   avoid overrepresentation of study cases with large numbers of data points (Table S3). The Fe_R-

365   OC/TOC data of different study areas are then grouped into four categories according to the

366   depositonal environments and used for one-way ANOVA and box-whisker plots.

Methods

Sediment core collection and age model establishment

The Qiongdongnan (QDN) basin lies in the rift belt of the northern continental margin

of the South China Sea and receives terrestrial material mainly from the Indo-China

Peninsula and Southeast China (especially Hainan Island) by river runoff and aeolian

dust[48, 49]. In addition, the material contribution of marine authigenic sources to the

basin cannot be neglected[49].

Core QDN-14B was recovered from the QDN basin at a water depth of 1370 m in

2015, ~600 m east of ROV1, which is an active seep site of "Haima" cold seeps[50].

Core QDN-G1 was recovered outside the area of "Haima" cold seeps around 35 km

away from QDN-14B at a water depth of 1478 m in 2018 (Fig. 1a). Sediment samples

were subsampled every 40 cm and preserved at -80 ℃. Known volumes of sediments

were taken using tip cut-off syringes and sealed in glass vials for further

measurements of density and porosity. For core QDN-G1, the age model of the upper

4.0 m was based on 7 accelerator mass spectrometry ^{14}C ages of planktonic

foraminifera (*G. ruber*) (Table S1). The age model of the lower part (4.0-10.8 m) was

established by aligning the benthic foraminifera (*C.wuellerstorfi*) δ^{18}O record to the

global benthic δ^{18}O stack LR04[21] (Fig. 1b).

Pore water sampling and analysis

Pore water samples were extracted immediately onboard using Rhizon samplers (0.22

389   μm filter) before the core was cut open for sediment subsampling. To prevent

390   oxidation of Fe(II), an aliquot of pore water was added to the ferrozine solution. Pore

391   water samples for dissolved inorganic carbon measurements were preserved in pre-

392   vacuumed glass vials. Pore water samples for ion measurements were acidified with

393   concentrated HNO_3. The rest of the pore water samples were preserved in pre-

394   combusted amber glass vials at $-20°C$ for dissolved organic carbon measurements.

395

396   The Fe(II) concentration was determined by ferrozine assay using a

397   spectrophotometer[51]. The concentrations of major cations and anions were determined

398   by ion chromatography (Dionex ICS-5000+). Dissolved inorganic carbon (DIC) was

399   measured using a total carbon analyzer (Multi 3100, Jena).

400

401   **Physical properties of bulk sediments**

402   Known volumes of sediments were subsampled by tip cut-off syringes and preserved

403   in sealed glass vials for the measurements of physical properties, such as porosity and

404   dry bulk density. All the physical properties were only measured for QDN-G1

405   samples. The averaged porosity and dry bulk density were used to represent the

406   general porosities of the two cores.

407

408   Porosity was calculated by the volume ratio of water and wet sediment, where the

409   volume of water was calculated from the difference between the wet and dry sample

410   weight. The dry bulk density was calculated by dividing the dry sample weight by the

411   original wet sample volume.

412

413   **Fe$_R$ and Fe$_R$−OC extraction**

414   Fe$_R$ and Fe$_R$-OC were extracted using the citrate-bicarbonate-dithionite (CBD)

415   method according to Mehra and Jackson (1960)[20], as modified by Lalonde et al.[1] and

416   Salvadó et al.[2]. Both poorly crystalline and crystalline iron (oxyhydr)oxides can be

417   reduced by this method, including mainly goethite and hematite, which are the major

418   iron (oxyhydr)oxides in marine sediments[52, 53]. Briefly, samples were freeze-dried and

419   homogenized using an agate mortar and pestle. Samples (0.5 g) were weighed

420   carefully into 40 mL Teflon tubes and extracted in a 30 mL solution of sodium

421   dithionite and trisodium citrate buffered with sodium bicarbonate at 80°C for 15 min

422   in a water bath. After the extraction, the suspensions were centrifuged for 10 min at

423   4000×g and then rinsed 5 times with artificial seawater. To evaluate the amount of OC

424   remobilized during the extraction that was not associated with Fe$_R$, another sample

425   aliquot was extracted as a control under the same experimental conditions, but

426   replacing sodium dithionite and trisodium citrate with sodium chloride with

427   equivalent ion strength. The residuals were dried overnight in a 50°C oven, carefully

428   weighed and manually ground.

429

430   The supernatant and rinse water were combined, acidified to pH<2 and filtered

431   through 0.22 μm filters. The dissolved iron was determined using a ferrozine assay[51].

432   The iron extracted in the control group were negligible; therefore, the amount of Fe$_R$

was calculated based on the iron extracted in the dithionite reduction group without

further correction.

Fe_R-OC quantification and carbon isotope analyses

The OC content and carbon isotope ratio were determined for both untreated and

treated samples using an elemental analyser (Vario EL III, Elementar) coupled to an

isotope ratio mass spectrometer (Isoprime, Elementar) at the instrumental analysis

centre, Shanghai Jiao Tong University. The inorganic carbon was removed by acid

fumigation before the analysis. The samples were measured in triplicate, and the

standard deviation was <0.05% for TOC and <0.2‰ for $\delta^{13}C$. The analytical precision

was <0.06% for TOC (standard deviation for repeated measurements of the low

organic content soil standard; n=3) and <0.09‰ for $\delta^{13}C$ (standard deviation for

repeated measurements of the USGS40 standard, n=3).

Calculation of Fe_R−OC percentage in TOC and $\delta^{13}C_{FeR-OC}$

The amount of Fe_R-OC was determined as the difference of TOC amount in the

residuals between the CBD extraction and control extraction.

Fe_R-OC percentage in TOC= (TOC$_{control}$- TOC$_{CBD}$)/TOC$_{bulk}$

in which,

TOC$_{control}$= total organic carbon (mg) left after the control extraction,

TOC$_{CBD}$= total organic carbon (mg) left after the CBD extraction,

TOC$_{bulk}$ = total organic carbon (mg) in the untreated sample.

455

A binary mixing model was used to calculate the carbon isotope ratio of Fe_R-OC,

where the OC pool in the residual of the control group ($TOC_{control}$) is comprised of

Fe_R-OC and OC remaining untouched after CBD extraction (TOC_{CBD}). The carbon

isotope ratios of Fe_R-OC was calculated according to the following mass-balanced

equations:

$TOC_{CBD} + Fe_R\text{-}OC = TOC_{control}$

$f TOC_{CBD} \times \delta^{13}C_{CBD} + f Fe_R\text{-}OC \times \delta^{13}C_{FeR\text{-}OC} = \delta^{13}C_{control}$

in which,

Fe_R-OC= the amount of organic carbon (mg) associated with Fe_R,

TOC_{CBD}= total organic carbon (mg) left after the CBD extraction,

$TOC_{control}$= total organic carbon (mg) left after the control extraction,

$f TOC_{CBD} = TOC_{CBD}/TOC_{control}$,

$f Fe_R\text{-}OC = Fe_R\text{-}OC/TOC_{control}$,

$\delta^{13}C_{CBD}$ = the measured carbon isotope signature of TOC_{CBD},

$\delta^{13}C_{control}$ = the measured carbon isotope signature of $TOC_{control}$,

$\delta^{13}C_{FeR\text{-}OC}$ = the carbon isotope signature of Fe_R-OC.

472

Geochemical modelling

Net reaction rates of sulfate were estimated using the MATLAB script published in

Wang et al., 2008[36], considering molecular diffusion, sediment burial, fluid advection,

476 and reaction under the assumption that the sulfate concentration profiles represent

477 steady-state conditions.

478 The mass balance of sulfate is expressed as:

479
$$-\frac{\partial}{\partial x}\left\{-\frac{D(x)}{\theta^2(x)}\frac{\partial[\emptyset(x)C(x)]}{\partial x} + [\emptyset(x)b(x) + \emptyset(x)v(x)]C(x)\right\} + R(x) = 0$$

480 Where $C(x)$ is sulfate concentration in the pore water, x is depth below the seafloor,

481 $\emptyset(x)$ is porosity, $D(x)$ is the molecular diffusion coefficient of sulfate, $\theta^2(x)$ is

482 tortuosity, $b(x)$ is pore water burial velocity, $v(x)$ is externally driven flow velocity,

483 $R(x)$ is the rate of diagenetic reaction per unit volume of sediment[36].

484

485 The model applied a 5-point Gaussian filter to the sulfate concentration profile, with

486 the weighting on the 5 points of: [0.06, 0.24, 0.4, 0.24, 0.06]. All parameters used for

487 modelling are listed in Table S2. Porosity profile was measured using QDN-G1

488 samples. The averaged porosity was applied as the constant porosity value for both

489 cores assuming similar sediment properties in the study area. Diffusion coefficients of

490 sulfate in the two cores were obtained using R package marelac[54] with the input of

491 respective salinity, temperature and pressure values (Table S2). The tortuosity θ^2 was

492 calculated by the relation, $\theta^2 = \emptyset f$, where f is the formation factor, which can be

493 calculated based on the empirical relationship $f = 1.3 \times \emptyset^{-1.45}$ [55, 56]. We used the

494 sedimentation rate near the seafloor 1.2×10^{-4} m yr^{-1} as the pore water burial velocity

495 for both cores, assuming a similar sedimentation rate in the study area, which is

496 calculated by the radiocarbon dating ages of the first two sampling layers below the

497 seafloor in QDN-G1. A constant external flow advection velocity near the sediment-

498   water interface of 10^{-5} m yr^{-1} was used[36]. A minimum of three measured

499   concentration data points were used to determine each reaction zone[36]. The model

500   quantifies uncertainties in the rate estimates by using a Monte Carlo technique[36]. The

501   depth-integrated net reaction rate yielded the total flux at steady state for the sediment

502   column.

503

504   **The accumulation rate of TOC and Fe$_R$-OC in QDN-14B**

505   The accumulation rate of TOC and Fe$_R$-OC were calculated as[57]:

506

507   TOC accumulation rate = LSR × DBD × TOC%

508

509   Fe$_R$-OC accumulation rate = LSR × DBD × Fe$_R$-OC%

510

511   where DBD is the dry sediment bulk density in g cm^{-3}, LSR is the linear

512   sedimentation rate in cm kyr^{-1}, TOC% and Fe$_R$-OC% are the weight percentage of

513   TOC and Fe$_R$-OC in sediments, respectively. The TOC and Fe$_R$-OC accumulation rate

514   is expressed in mol m^{-2} kyr^{-1}. The average sedimentation rate (11.1 cm kyr^{-1}) and the

515   average dry bulk density (0.9 g cm^{-3}) of QDN-G1 was used for the calculation for

516   core QDN-14B, assuming similar sedimentation rate and bulk sediment properties in

517   the study area.

518

519   **DNA extraction, qPCR and amplicon sequencing**

520   The 16S rRNA gene data was obtained for core QDN-G1 according to the following

521   procedures.

522

523 The DNA for qPCR and V4 region of 16S rRNA gene sequencing was extracted from

524 ~0.25 g of sediments using DNeasy® PowerSoil® Pro Kit (Qiagen), according to the

525 manufacturer's instructions.

526

527 The extracted DNA was used as template for qPCR to determine the abundance of

528 bacterial 16S rRNA gene with the primer set 331F/797R [58]. Standard curves were

529 constructed using a 10-fold series dilution of the plasmids for six gradients carrying

530 the bacteria 16S rRNA gene. qPCR was carried out in a volume of 20 μL, including

531 10 μL 2 × PowerUp™ SYBR™ Green Master Mix (Thermo Fisher), 1.6 μL each

532 primer (10 μM), 2 μL template DNA and 4.8 μL steriled deionized water. The qPCR

533 program consisted of an initial cycle of 95 °C for 5 min; 40 cycles of 95 °C for 30 s,

534 60 °C for 30 s, 72 °C for 30 s, 80 °C for 10 s, and the data was collected at the final

535 step of each cycle. The melting curve was generated using default program. All

536 samples were subject to qPCR measurement with three technical replicates. The

537 bacterial cell number was evaluated based on the abundance of 16S rRNA gene,

538 applying the average copy number of the 16S rRNA gene on genomes of Bacteria (5.3

539 copies/genome, rrnDB version 5.8)[59].

540

541 The V4 region of 16S rRNA gene was amplified using the primer set 515F/806R[60].

542 DNA was amplified using the following cycling conditions: 95°C, 5 min; 30 cycles

543 (95°C, 30 s; 50°C, 30 s; 72°C, 30 s); 72°C, 7 min. The PCR products of samples were

544   sent to Shanghai Personal Biotechnology Co., Ltd. (Shanghai, China) for high-

545   throughput sequencing of the 16S rRNA gene using the Illumina Novaseq PE250

546   platform.

547

548   **Sequence analysis**

549   The raw reads of 16S rRNA gene of both cores QDN-G1 and QDN-14B were

550   processed and analyzed using the QIIME 2 platform (version 2020.11)[61]. The primers

551   and adaptors were first trimmed out using Cutadapt (version 3.1)[62]. Raw sequences

552   were then processed using DADA2[63], including quality filtering, denoising, paired-

553   end sequence merging, chimera filtering and producing amplicon sequence variants

554   (ASVs) and ASV Table. Taxonomy was assigned using q2-feature-classifier (a scikit-

555   learn naive Bayes machine-learning classifier)[64] with Silva database release 138[65].

556   Multiple sequence alignment and phylogenetic tree construction were performed

557   using the QIIME 2 plugin q2-phylogeny (align-to-tree-mafft-iqtree). Unassigned

558   sequences, singletions and sequences affiliated with eukaryotes were discarded.

559   Eventually, to eliminate uneven sequencing depths, the ASV table was rarefied to

560   14935 and 71773 sequences per sample for QDN-14B and QDN-G1, respectively,

561   determined by the sample with the fewest sequences.

562

563   **Data availability**

564   Raw Illumina sequence data of the 16S rRNA gene generated for cores QDN-14B and QDN-G1 in

565   this study has been deposited in the NODE (the National Omics Data Encyclopedia,

569   **References**

570   1.   Lalonde, K., Mucci, A., Ouellet, A. & Gélinas, Y. Preservation of organic matter
571   in sediments promoted by iron. *Nature* **483**, 198-200 (2012).
572   2.   Salvadó, J. A. et al. Organic carbon remobilized from thawing permafrost is
573   resequestered by reactive iron on the Eurasian Arctic Shelf. *Geophys. Res. Lett.*
574   **42**, 8122-8130 (2015).
575   3.   Barber, A. et al. Preservation of organic matter in marine sediments by inner-
576   sphere interactions with reactive iron. *Sci. Rep.* **7**, 366 (2017).
577   4.   Kaiser, K. & Guggenberger, G. The role of DOM sorption to mineral surfaces
578   in the preservation of organic matter in soils. *Org. Geochem.* **31**, 711-725 (2000).
579   5.   Mikutta, R., Kleber, M., Torn, M. S. & Jahn, R. Stabilization of soil organic
580   matter: association with minerals or chemical recalcitrance? *Biogeochemistry*
581   **77**, 25-56 (2006).
582   6.   Jones, D. & Edwards, A. Influence of sorption on the biological utilization of
583   two simple carbon substrates. *Soil Biol. Biochem.* **30**, 1895-1902 (1998).
584   7.   Eusterhues, K., Neidhardt, J., Hädrich, A., Küsel, K. & Totsche, K. U.
585   Biodegradation of ferrihydrite-associated organic matter. *Biogeochemistry* **119**,
586   45-50 (2014).
587   8.   Zhao, B. et al. The Role of Reactive Iron in the Preservation of Terrestrial
588   Organic Carbon in Estuarine Sediments. *J. Geophys. Res. Biogeosci.* **123**,
589   https://doi.org/10.1029/2018JG004649 (2018).
590   9.   Canfield, D. E. & Thamdrup, B. Towards a consistent classification scheme for
591   geochemical environments, or, why we wish the term 'suboxic'would go away.
592   *Geobiology* **7**, 385-392 (2009).
593   10.   Froelich, P. N. et al. Early oxidation of organic matter in pelagic sediments of
594   the eastern equatorial Atlantic: suboxic diagenesis. *Geochim. Cosmochim. Acta*
595   **43**, 1075-1090 (1979).
596   11.   Adhikari, D. et al. Asynchronous reductive release of iron and organic carbon
597   from hematite–humic acid complexes. *Chem. Geol.* **430**, 13-20 (2016).
598   12.   Zhao, Q. et al. Coupled dynamics of iron and iron-bound organic carbon in
599   forest soils during anaerobic reduction. *Chem. Geol.* **464**, 118-126 (2017).
600   13.   Zeng, Q. et al. Bio-reduction of ferrihydrite-montmorillonite-organic matter
601   complexes: Effect of montmorillonite and fate of organic matter. *Geochim.*
602   *Cosmochim. Acta* **276**, 327-344 (2020).
603   14.   Patzner, M. S. et al. Iron mineral dissolution releases iron and associated organic
604   carbon during permafrost thaw. *Nat. Commun.* **11**, 6329 (2020).
605   15.   Faust, J. C. et al. Millennial scale persistence of organic carbon bound to iron in

606   Arctic marine sediments. *Nat. Commun.* **12**, 275 (2021).

607   16.   Shields, M. R., Bianchi, T. S., Gélinas, Y., Allison, M. A. & Twilley, R. R.
608   Enhanced terrestrial carbon preservation promoted by reactive iron in deltaic
609   sediments. *Geophys. Res. Lett.* **43**, 1149-1157 (2016).

610   17.   Sun, C.-H. et al. Examining bulk and iron-associated organic carbon through
611   depth in margin sea sediments (China) under contrasting depositional settings:
612   Chemical and NEXAFS spectral characterization. *J. Mar. Syst.* **207**, 103344
613   (2020).

614   18.   Berner, R. A. GEOCARBSULF: A combined model for Phanerozoic
615   atmospheric O2 and CO2. *Geochim. Cosmochim. Acta* **70**, 5653-5664 (2006).

616   19.   Niu, M., Fan, X., Zhuang, G., Liang, Q. & Wang, F. Methane-metabolizing
617   microbial communities in sediments of the Haima cold seep area, northwest
618   slope of the South China Sea. *FEMS Microbiol. Ecol.* **93**, fix101 (2017).

619   20.   Mehra, O. & Jackson, M. Iron oxide removal from soils and clays by a
620   dithionite-citrate system buffered with sodium bicarbonate. *Clays Clay Miner.*
621   **7**, 317-327 (1960).

622   21.   Lisiecki, L. E. & Raymo, M. E. A Pliocene‐Pleistocene stack of 57 globally
623   distributed benthic δ18O records. *Paleoceanography* **20**, PA1003 (2005).

624   22.   Wang, X. et al. Using chemical compositions of sediments to constrain methane
625   seepage dynamics: A case study from Haima cold seeps of the South China Sea.
626   *J. Asian Earth Sci.* **168**, 137-144 (2018).

627   23.   He, B. et al. Sources and accumulation of organic carbon in the Pearl River
628   Estuary surface sediment as indicated by elemental, stable carbon isotopic, and
629   carbohydrate compositions. *Biogeosciences* **7**, 3343-3362 (2010).

630   24.   Yoshinaga, M. Y. et al. Carbon isotope equilibration during sulphate-limited
631   anaerobic oxidation of methane. *Nat. Geosci.* **7**, 190-194 (2014).

632   25.   Boetius, A. et al. A marine microbial consortium apparently mediating
633   anaerobic oxidation of methane. *Nature* **407**, 623-626 (2000).

634   26.   Egger, M., Riedinger, N., Mogollón, J. M. & Jørgensen, B. B. Global diffusive
635   fluxes of methane in marine sediments. *Nat. Geosci.* **11**, 421-425 (2018).

636   27.   Dos Santos Afonso, M. & Stumm, W. Reductive dissolution of iron (III)(hydr)
637   oxides by hydrogen sulfide. *Langmuir* **8**, 1671-1675 (1992).

638   28.   Canfield, D. E., Raiswell, R. & Bottrell, S. H. The reactivity of sedimentary iron
639   minerals toward sulfide. *Am. J. Sci.* **292**, 659-683 (1992).

640   29.   Lovley, D. R., Roden, E. E., Phillips, E. J. P. & Woodward, J. C. Enzymatic iron
641   and uranium reduction by sulfate-reducing bacteria. *Mar. Geol.* **113**, 41-53
642   (1993).

643   30.   Li, Y.-L., Vali, H., Yang, J., Phelps, T. J. & Zhang, C. L. Reduction of iron oxides
644   enhanced by a sulfate-reducing bacterium and biogenic H2S. *Geomicrobiol. J.*
645   **23**, 103-117 (2006).

646   31.   Cai, C. et al. A methanotrophic archaeon couples anaerobic oxidation of
647   methane to Fe (III) reduction. *ISME J.* **12**, 1929-1939 (2018).

648   32.   Wang, X.-C., Druffel, E. R., Griffin, S., Lee, C. & Kashgarian, M. Radiocarbon
649   studies of organic compound classes in plankton and sediment of the

northeastern Pacific Ocean. *Geochim. Cosmochim. Acta* **62**, 1365-1378 (1998).

33. Yang, S. et al. Genomic and enzymatic evidence of acetogenesis by anaerobic methanotrophic archaea. *Nat. Commun.* **11**, 3941 (2020).

34. Kaiser, K. & Guggenberger, G. Sorptive stabilization of organic matter by microporous goethite: sorption into small pores vs. surface complexation. *Eur. J. Soil Sci.* **58**, 45-59 (2007).

35. Wagai, R. & Mayer, L. M. Sorptive stabilization of organic matter in soils by hydrous iron oxides. *Geochim. Cosmochim. Acta* **71**, 25-35 (2007).

36. Wang, G., Spivack, A. J., Rutherford, S., Manor, U. & D'Hondt, S. Quantification of co-occurring reaction rates in deep subseafloor sediments. *Geochim. Cosmochim. Acta* **72**, 3479-3488 (2008).

37. Müller, A. L., Kjeldsen, K. U., Rattei, T., Pester, M. & Loy, A. Phylogenetic and environmental diversity of DsrAB-type dissimilatory (bi) sulfite reductases. *ISME J.* **9**, 1152-1165 (2015).

38. Hedges, J. I. & Keil, R. G. Sedimentary organic matter preservation: an assessment and speculative synthesis. *Mar. Chem.* **49**, 81-115 (1995).

39. LaRowe, D. E. et al. Organic carbon and microbial activity in marine sediments on a global scale throughout the Quaternary. *Geochim. Cosmochim. Acta* **286**, 227-247 (2020).

40. Kallmeyer, J., Pockalny, R., Adhikari, R. R., Smith, D. C. & D'Hondt, S. Global distribution of microbial abundance and biomass in subseafloor sediment. *Proc. Natl. Acad. Sci.* **109**, 16213-16216 (2012).

41. Riedel, T., Zak, D., Biester, H. & Dittmar, T. Iron traps terrestrially derived dissolved organic matter at redox interfaces. *Proc. Natl. Acad. Sci.* **110**, 10101-10105 (2013).

42. Shen, J. et al. Laterally transported particles from margins serve as a major carbon and energy source for dark ocean ecosystems. *Geophys. Res. Lett.* **47**, e2020GL088971 (2020).

43. Ran, L. et al. Sediment Resuspension as a Major Contributor to Sinking Particles in the Northwestern South China Sea: Evidence From Observations and Modeling. *Front. Mar. Sci.* **9**, 819340 (2022).

44. Friedlingstein, P. et al. Global carbon budget 2021. *Earth System Science Data* **14**, 1917-2005 (2022).

45. Holmkvist, L., Ferdelman, T. G. & Jørgensen, B. B. A cryptic sulfur cycle driven by iron in the methane zone of marine sediment (Aarhus Bay, Denmark). *Geochim. Cosmochim. Acta* **75**, 3581-3599 (2011).

46. Liang, L. et al. Iron (oxyhydr)oxides shift the methanogenic community in deep sea methanic sediment - insights from long-term high-pressure incubations. *Sci. Total Environ.* **848**, 157590 (2022).

47. Contreras, S. et al. Cyclic 100-ka (glacial-interglacial) migration of subseafloor redox zonation on the Peruvian shelf. *Proc. Natl. Acad. Sci.* **110**, 18098-18103 (2013).

48. Zhao, Z. et al. The high resolution sedimentary filling in Qiongdongnan Basin, Northern South China Sea. *Mar. Geol.* **361**, 11-24 (2015).

694 49. Liu, X. et al. A heavy mineral viewpoint on sediment provenance and
695 environment in the Qiongdongnan Basin. *Acta Oceanologica Sinica* **34**, 41-55
696 (2015).

697 50. Hu, Y. et al. Pore fluid compositions and inferred fluid flow patterns at the
698 Haima cold seeps of the South China Sea. *Mar. Pet. Geol.* **103**, 29-40 (2019).

699 51. Stookey, L. L. Ferrozine---a new spectrophotometric reagent for iron. *Anal.*
700 *Chem.* **42**, 779-781 (1970).

701 52. van der Zee, C., Roberts, D. R., Rancourt, D. G. & Slomp, C. P. Nanogoethite
702 is the dominant reactive oxyhydroxide phase in lake and marine sediments.
703 *Geology* **31**, 993-996 (2003).

704 53. Zhang, Y. G., Ji, J., Balsam, W. L., Liu, L. & Chen, J. High resolution hematite
705 and goethite records from ODP 1143, South China Sea: Co-evolution of
706 monsoonal precipitation and El Niño over the past 600,000 years. *Earth Planet.*
707 *Sci. Lett.* **264**, 136-150 (2007).

708 54. Soetaert, K., Petzoldt, T. & Meysman, F. marelac: Tools for Aquatic Sciences.
709 R package version 2.1 http://CRAN.R-project.org/package=marelac (2010).

710 55. Boyce, R. E. Electrical resistivity of modern marine sediments from the Bering
711 Sea. *J. Geophys. Res.* **73**, 4759-4766 (1968).

712 56. Breitzke, M. Physical Properties of Marine Sediments. In: *Marine*
713 *Geochemistry* (eds Schulz HD, Zabel M). Springer Berlin Heidelberg (2006).

714 57. Xu, Y. et al. Distribution, Source, and Burial of Sedimentary Organic Carbon in
715 Kermadec and Atacama Trenches. *J. Geophys. Res. Biogeosci.* **126**,
716 e2020JG006189. doi: 006110.001029/002020JG006189 (2021).

717 58. Santelli, C. M. et al. Abundance and diversity of microbial life in ocean crust.
718 *Nature* **453**, 653-656 (2008).

719 59. Stoddard, S. F., Smith, B. J., Hein, R., Roller, B. R. K. & Schmidt, T. M. rrnDB:
720 improved tools for interpreting rRNA gene abundance in bacteria and archaea
721 and a new foundation for future development. *Nucleic Acids Res.* **43**, D593-
722 D598 (2014).

723 60. Caporaso, J. G. et al. Global patterns of 16S rRNA diversity at a depth of
724 millions of sequences per sample. *Proc. Natl. Acad. Sci.* **108**, 4516-4522 (2011).

725 61. Bolyen, E. et al. Reproducible, interactive, scalable and extensible microbiome
726 data science using QIIME 2. *Nat. Biotechnol.* **37**, 852-857 (2019).

727 62. Martin, M. Cutadapt removes adapter sequences from high-throughput
728 sequencing reads. *EMBnet.journal* **17**, 10-12 (2011).

729 63. Callahan, B. J. et al. DADA2: high-resolution sample inference from Illumina
730 amplicon data. *Nat. Methods* **13**, 581-583 (2016).

731 64. Bokulich, N. A. et al. Optimizing taxonomic classification of marker-gene
732 amplicon sequences with QIIME 2's q2-feature-classifier plugin. *Microbiome*
733 **6**, 1-17 (2018).

734 65. Quast, C. et al. The SILVA ribosomal RNA gene database project: improved
735 data processing and web-based tools. *Nucleic Acids Res.* **41**, D590-D596 (2012).

736

Author contributions

F.W designed the research and secured funding. Y.C. collected geochemical data, performed data analysis, and wrote the first draft of the manuscript. L.D constructed the age model. W.S and M.N. collected and analyzed microbial data. All authors discussed the results and commented on the manuscript.

Competing interests

The authors declare no competing interests.

Materials & Correspondence

Prof. Fengping Wang

School of Oceanography, Shanghai Jiao Tong University, Shanghai, China

Email: fengpingw@sjtu.edu.cn

Supplementary Information for

Reactive iron as an important reservoir of marine organic carbon over geological timescales

Yunru Chen[1], Liang Dong[2], Weikang Sui[2], Mingyang Niu[1], Xingqian Cui[2], Kai-Uwe Hinrichs[4], Fengping Wang[2,3]*

1. State Key Laboratory of Microbial Metabolism, School of Life Sciences and Biotechnology, Shanghai Jiao Tong University, Shanghai 200240, China

2. School of Oceanography, Shanghai Jiao Tong University, Shanghai 200240, China

3. Southern Marine Science and Engineering Guangdong Laboratory (Zhuhai), Zhuhai 519000, China

4. MARUM-Center for Marine Environmental Sciences and Department of Geosciences, University of Bremen, D-28359 Bremen, Germany

*Correspondence: fengpingw@sjtu.edu.cn

This file includes:

Supplementary Text

Table S1 to S4

Fig. S1 to S5

References

Supplementary Text

Variations of TOC and Fe$_R$-OC records over glacial/interglacial cycles

Because of relatively weak microbial activities and well-established age model, core QDN-G1, representing typical continental slope sediments, is used to constrain the variation of TOC and Fe$_R$-OC records controlled by environmental changes across glacial/interglacial cycles.

In global marine sediments, except polar regions, the burial of OC has natural variations over glacial/interglacial cycles, with much higher accumulation rate in glacials than during interglacials for higher marine primary productivity and more efficient preservation[1]. If the environmental factors being the main controlling factor of OC content, higher content should be expected in glacials. However, in core QDN-G1, we found consistently low TOC and Fe$_R$-OC content across MIS5 (interglacial) and MIS4 (glacial) (Figure S4b).

The variations in the carbon isotope ratio of OC in marine sediments are generally ascribed to three reasons: variable contribution of terrestrial- and marine-sourced OC (sediment provenance), variable isotope composition of marine-sourced OC and selective microbial degradation after deposition[2]. If the carbon isotope ratio reflects the relative contribution of terrestrial and marine OC, it should be in lower in MIS 2 and MIS 4, when the sea-level stand was at least 40 meters lower than that in MIS 5 (Fig. S4e) and terrestrial supply was higher for the closer river mouth to the study sites[3].

804   However, the carbon isotope ratio of TOC and Fe_R-OC were consistently depleted

805   during MIS 5 to MIS 4 and became more enriched during MIS 3 to 1 (Figure. S4c).

806   Therefore, the variations can be hardly explained by the changes in sediment

807   provenance. If it reflects variation in the isotope composition of marine OC, we should

808   also expect lower values in interglacials (MIS 1 and MIS 5) and lower values in glacial

809   (MIS 2 and MIS 4)[4]. Similarly, this possibility is also ruled out.

810

811   Collectively, the distinctive low content and depleted carbon isotope ratio of TOC and

812   Fe_R-OC can be hardly explained by the controlling of environmental changes before

813   deposition on glacial/interglacial timescales.

814
815

816   Table S1. AMS ^{14}C age control points used to reconstruct the age model of core QDN-

817   G1

Depth (cmbsf)	AMS ^{14}C age (BP)	Error	Calendar Age (cal BP)	Dating foraminifera species
0	2030	±30	1603	*G. ruber*
80	8090	±30	8538	*G. ruber*
120	10500	±30	11657	*G. ruber*
200	14050	±40	16457	*G. ruber*
280	21070	±70	24878	*G. ruber*
360	27450	±120	31069	*G. ruber*
400	30810	±170	34387	*G. ruber*

818
819

820   Table S2. The input parameters for geochemical modelling of net sulfate reaction rate

821   after the MATLAB script of Wang et al. 2008[5].

Parameters	Value for core QDN-G1	Value for core QDN-14B	Unit
Porosity	0.7	0.7	\
Formation factor	2.2	2.2	\
Sedimentary rate near the seafloor	0.000115	0.000115	$m\ yr^{-1}$
Diffusivity	0.0175	0.0175	$m^2\ yr^{-1}$
External flow advection velocity	0.00001	0.00001	$m\ yr^{-1}$
Significance level (F-test)	0.05	0.05	\
Minimum number of measured data within each reaction zone	3	3	\
Relative precision of concentration measurements	0.01	0.01	\
Number of random concentration profiles to estimate the uncertainty of reaction rates	50	50	\
Temperature	4	4	°C
Pressure	147.8	137.0	bar
Salinity	35	35	\
Water depth	1478	1370	m
Dry bulk density	0.9	0.9	$g\ cm^{-3}$

822

823 Table S3. Compilation of Fe_R-OC/TOC data in different marine environments. The
824 data are presented as means ± standard deviation for each study area.
825

Marine environments	Study area	Average Fe_R-OC/TOC (%)	Number of data points	Reference
Delta/Estuary	Changjiang Estuary	11.3±3.6	5	Zhao et al., 2018[6]
	Changjiang Estuary	5.7±2.3	9	Sun et al., 2020[7]
	Wax Lake Delta	15.1±8.7	37	Shields et al., 2016[8]
	Washington Coast	24.4±8.4	8	Lalonde et al., 2012[9]
	St-Lawrence Estuary	23.1±2.4	3	Lalonde et al., 2012[9]
	St-Lawrence Gulf	23.0±6.0	2	Lalonde et al., 2012[9]
	Mackenzie River delta	7.6	1	Lalonde et al., 2012[9]
Continental shelf (water depth<200 m)	East China Sea	13.2±8.9	12	Ma et al., 2018[10]
	South Yellow Sea	8.8±7.7	10	Ma et al., 2018[10]
	East China Sea Mobile-muds Zone	6.1±2.1	26	Zhao et al., 2018[6]
	East China Sea offshore	9.4±5.1	7	Zhao et al., 2018[6]
	Eurasian Arctic Shelf	11.0±5.5	29	Salvado et al., 2015[11]
	Bohai Sea	11.5±8.3	20	Wang et al., 2019[12]
	South Yellow Sea	13.0±7.4	27	Tao et al., 2017[13]
	South Yellow Sea	8.7±4.7	10	Sun et al., 2020[7]
	Barents Sea	18.9±7.6	127	Faust et al., 2020, 2021[14, 15]
Continental slope and deep sea (water depth>200 m)	Southern Ocean	29.0	1	Lalonde et al., 2012[9]
	Station M	14.3±4.1	2	Lalonde et al., 2012[9]
	Equatorial Pacific 0°N	34.8	1	Lalonde et al., 2012[9]
	Equatorial Pacific 9°N	12.2	1	Lalonde et al., 2012[9]
	Madeira turbidite	29.8	1	Lalonde et al., 2012[9]
	Arabian Sea	22.8±5.7	2	Lalonde et al., 2012[9]
	Mexican Margin	16.2±7.1	9	Lalonde et al., 2012[9]
	Okinawa Trough	8.6±3.5	8	Sun et al., 2020[7]
	South China Sea[a]	13.3±3.2	57	This study
Anoxic/sulfidic regions	Black Sea	15.9±12.8	2	Lalonde et al., 2012[9]
	Indian Margin	26.6	1	Lalonde et al., 2012[9]

Marine environments	Study area	Average Fe_R-OC/TOC (%)	Number of data points	Reference
Anoxic/sulfidic regions	Saanich inlet	28.1	1	Lalonde et al., 2012[9]
	Arabian Sea	22.8±5.7	2	Lalonde et al., 2012[9]
	Mexican margin	21.2±2.4	3	Lalonde et al., 2012[9]

826   [a]Data derived from SMTZ sediments in QDN-14B in this study are excluded from the

827   calculations, as they are affected by especially strong early diagenesis processes.

828   Table S4. Global budget of Fe_R-OC (10^{17} g C) in microbially reactive Quaternary
829   sediments. The Fe_R-OC budget was calculated by multiplying the TOC budget in these
830   two marine environments by the corresponding average Fe_R-OC/TOC ratio in surface
831   sediments, with the assumption that the percentage of Fe_R-OC in TOC stays mostly
832   stable during early diagenesis and can persist over geological timescales.

	Estuary and continental shelf (water depth < 200 m)	Continental slope and deep sea (water depth > 200 m)	Total
TOC budget[a]	20.4	1435	
Fe_R-OC/TOC (%)	13.2±6.1	20.1±9.3	
Fe_R-OC budget	2.7±1.2	288±133	291±133

833   [a]Data from LaRowe et al., 2020[16], where global datasets, including bathymetry,
834   sedimentation rates, POC content at the sediment-water interface and POC reactivity
835   were used to model the distribution of organic carbon in Quaternary marine sediments.

836

837

838
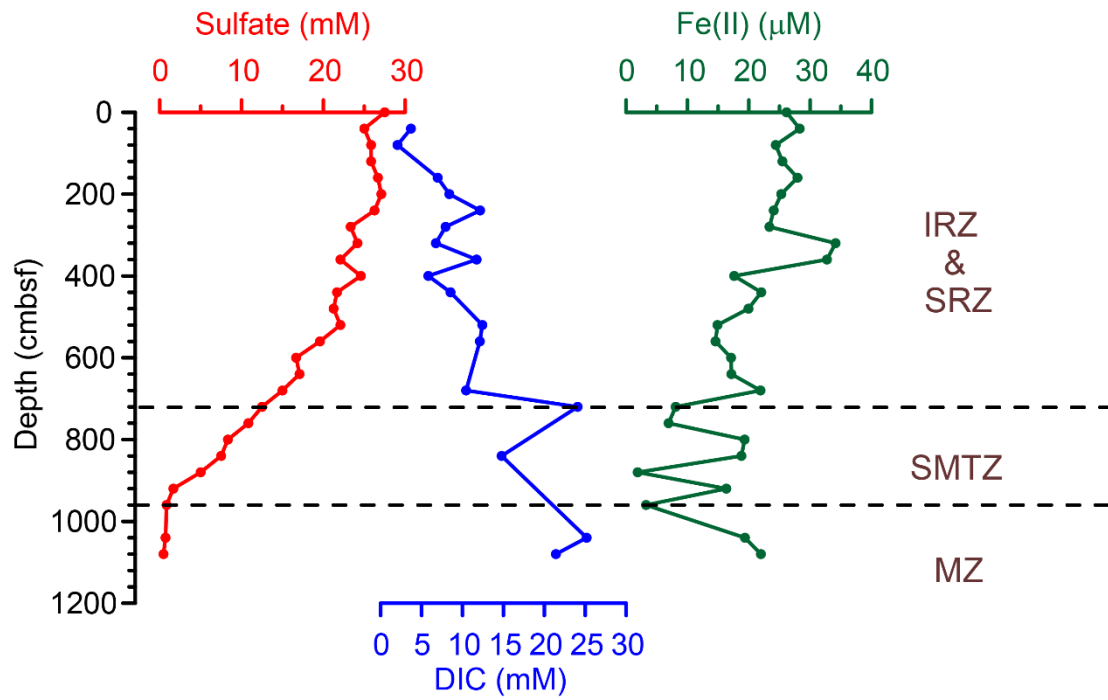
Fig. S1. Pore water geochemistry in core QDN-G1. Sulfate, DIC and Fe(II) concentrations are

presented to estimate the location of geochemical horizons, i.e., the iron reduction zone (IRZ), the

sulfate reduction zone (SRZ), the sulfate-methane transition zone (SMTZ), and the methanogenic

zone (MZ). The low concentrations of Fe(II) are consistent with precipitation of Fe(II) with sulfide

produced during sulfate reduction, indicating overlapped IRZ and SRZ. Given the data available,

the potential upper boundary of SMTZ was determined by abrupt increased DIC at 720 cmbsf. The

lower boundary of SMTZ was determined by the depletion of sulfate at 960 cmbsf.

846

847
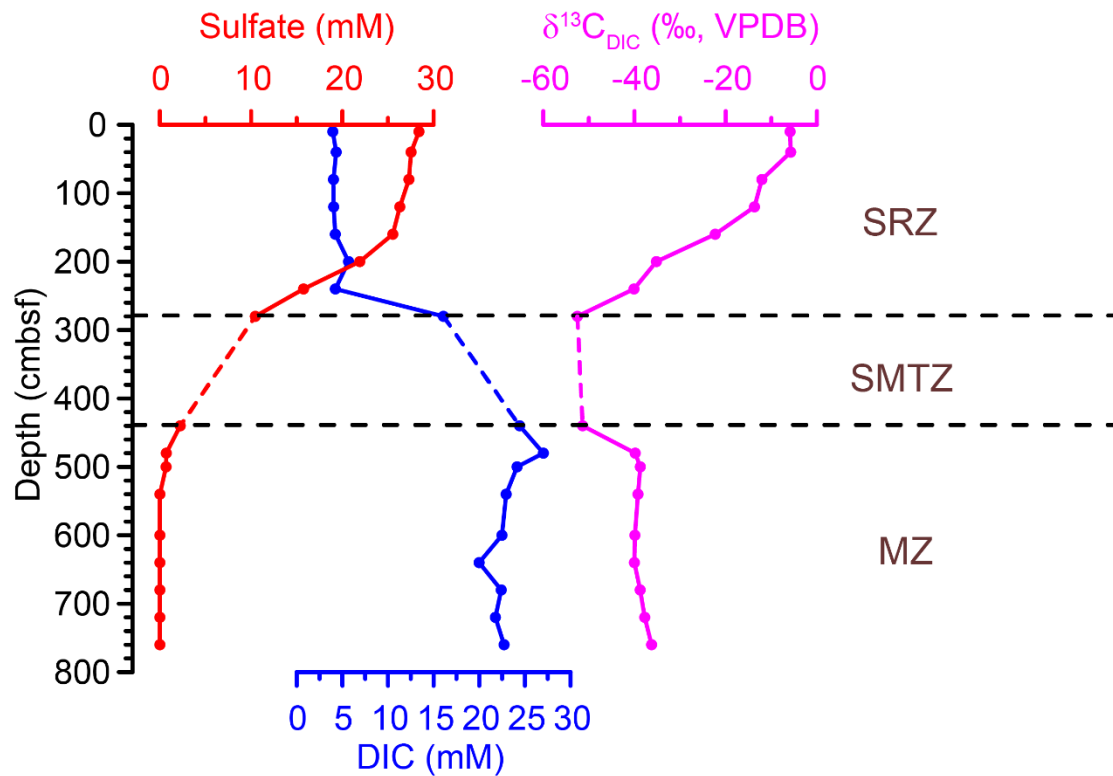
Fig. S2. Pore water geochemistry in core QDN-14B. Sulfate concentration, DIC concentration, and DIC carbon isotope ratio ($\delta^{13}C_{DIC}$) are presented to estimate the location of geochemical horizons, i.e., sulfate reduction zone (SRZ), sulfate-methane transition zone (SMTZ), and methanogenic zone (MZ). The estimated upper boundary of SMTZ was determined by increasing DIC concentration and depleted $\delta^{13}C_{DIC}$ at 280 cmbsf. The lower boundary of SMTZ was determined by the depletion of sulfate and depleted $\delta^{13}C_{DIC}$ at 440 cmbsf. All the data have been published in Hu et al. (2019)[17]. The data between 300 and 400 cmbsf were suspected to be influenced by seawater during core recovery, and are therefore not presented.

858

859
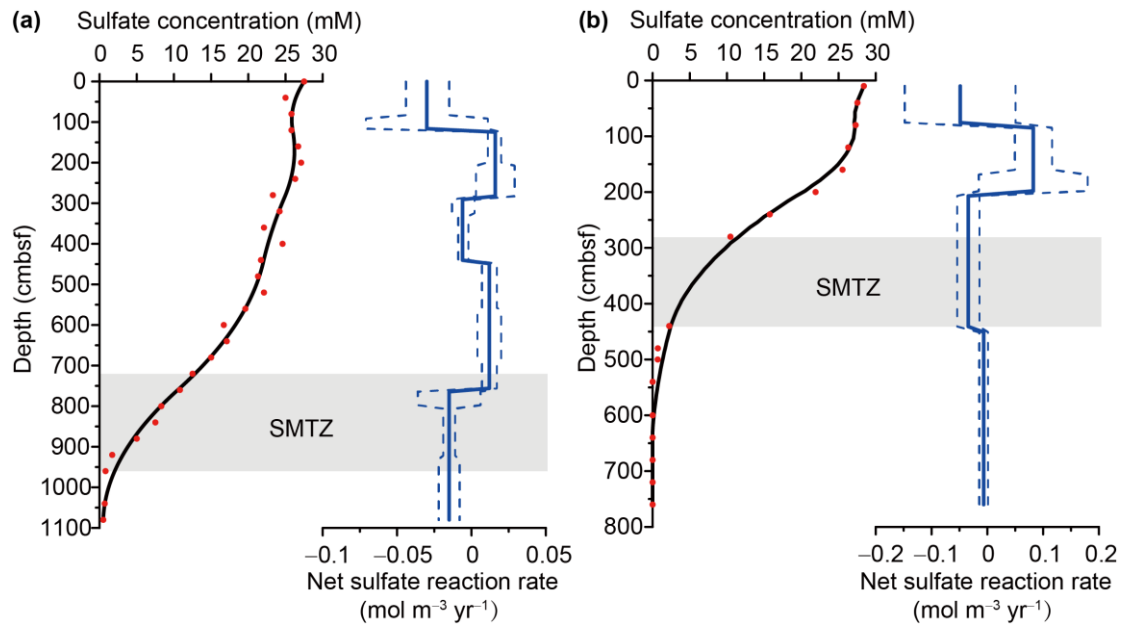
Fig. S3. Geochemical modelling of net sulfate reaction rate in cores QDN-G1 (a) and QDN-

14B (b). Negative values indicate net consumption, and positive values indicate net production. The

net sulfate reduction rate in SMTZ in QDN-14B is more than two times higher than that in QDN-

G1.

864
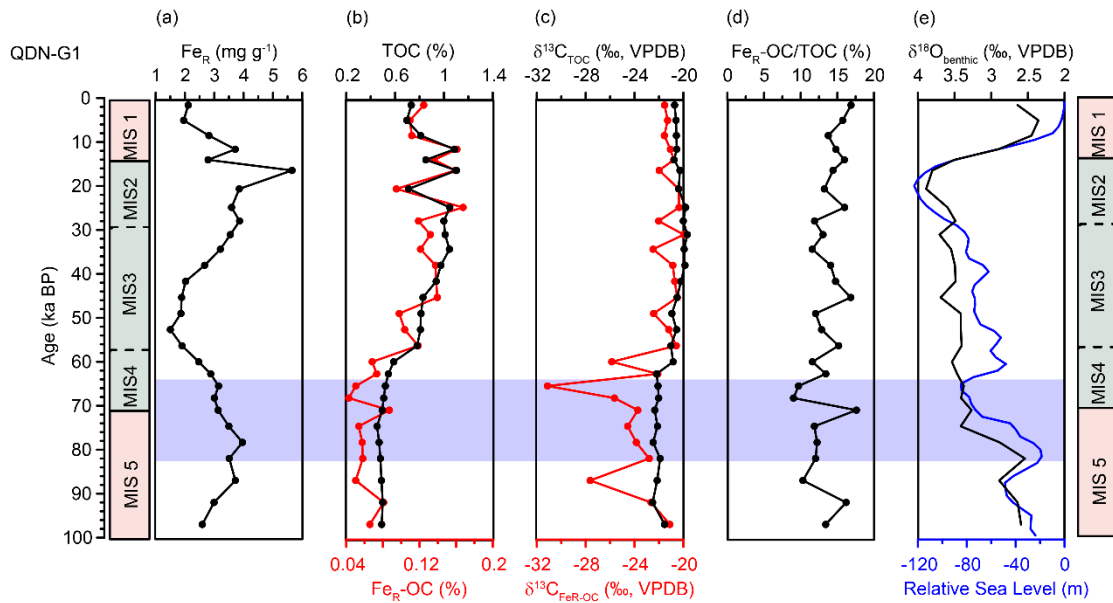
Fig. S4. Content and carbon isotope ratios of TOC and Fe$_R$-OC in core QDN-G1 over glacial/interglacial cycles. The pink and green bars indicate interglacial periods and the last glacial period, respectively. (a) Content of Fe$_R$. (b) Content of TOC (black line) and Fe$_R$-OC (red line). (c) Carbon isotope ratios of TOC (black line) and Fe$_R$-OC (red line). (d) Percentage of Fe$_R$-OC in TOC. (e) δ^{18}O record of benthic foraminifera (black line) and global relative sea level record from Waelbroeck et al, 2002[18] (blue line). The location of the SMTZ is highlighted in purple.

873
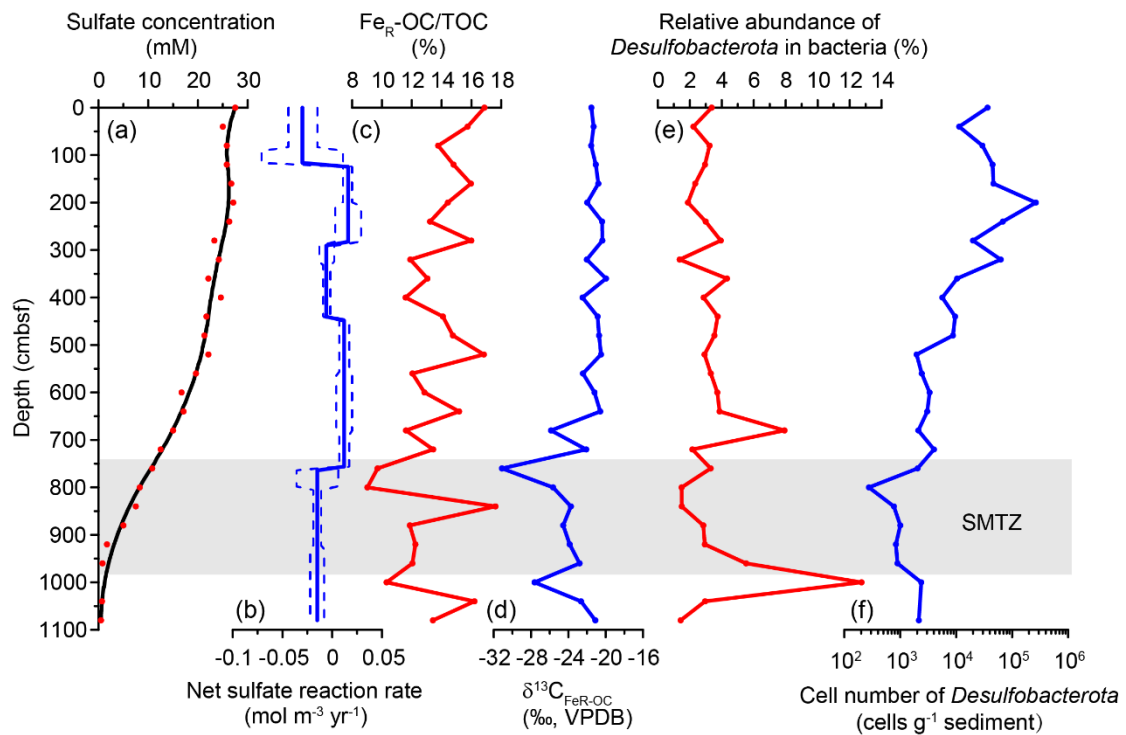
874

875 **Fig. S5. Geochemical modelling and microbial evidence show that low sulfate reduction rate**

876 **results in moderate decrease in Fe$_R$-OC in the SMTZ of core QDN-G1.** (a) Measured (red dots)

877 and fitted (black line) sulfate concentrations. A 5-point Gaussian filter was applied to the

878 concentration with the weighting on the 5 points of: [0.06, 0.24, 0.4, 0.24, 0.06][5]. (b) Modelled net

879 reaction rate profile of sulfate. Negative values indicate net consumption, and positive values

880 indicate net production. The 1 σ uncertainty envelope is shown in dashed line. (c) Down-core record

881 of Fe$_R$-OC/TOC. (d) Down-core record of $\delta^{13}C_{FeR-OC}$. (e) Relative abundance of *Desulfobacterota*

882 in bacteria, which is the phylum most of the sulfate-reducing bacteria belong to[19]. (f) The cell

883 number of *Desulfobacterota*, translated from the cell number of bacteria by multiplying the relative

884 abundance of *Desulfobacterota* in bacteria. The gray bar shows the position of SMTZ.

885

References

1. Cartapanis, O., Bianchi, D., Jaccard, S. L. & Galbraith, E. D. Global pulses of organic carbon burial in deep-sea sediments during glacial maxima. *Nat. Commun.* **7**, 10796 (2016).

2. Fontugne, M. R. & Calvert, S. E. Late Pleistocene Variability of the Carbon Isotopic Composition of Organic Matter in the Eastern Mediterranean: Monitor of Changes in Carbon Sources and Atmospheric CO2 Concentrations. *Paleoceanography* **7**, 1-20 (1992).

3. He, J., Zhao, M., Li, L., Wang, P. & Ge, H. Sea surface temperature and terrestrial biomarker records of the last 260 ka of core MD05-2904 from the northern South China Sea. *Chin. Sci. Bull.* **53**, 2376-2384 (2008).

4. Kienast, M., Calvert, S. E., Pelejero, C. & Grimalt, J. O. A critical review of marine sedimentary δ13Corg-pCO2 estimates: New palaeorecords from the South China Sea and a revisit of other low-latitude δ13Corg-pCO2 records. *Global Biogeochemical Cycles* **15**, 113-127 (2001).

5. Wang, G., Spivack, A. J., Rutherford, S., Manor, U. & D'Hondt, S. Quantification of co-occurring reaction rates in deep subseafloor sediments. *Geochim. Cosmochim. Acta* **72**, 3479-3488 (2008).

6. Zhao, B. et al. The Role of Reactive Iron in the Preservation of Terrestrial Organic Carbon in Estuarine Sediments. *J. Geophys. Res. Biogeosci.* **123**, https://doi.org/10.1029/2018JG004649 (2018).

7. Sun, C.-H. et al. Examining bulk and iron-associated organic carbon through depth in margin sea sediments (China) under contrasting depositional settings: Chemical and NEXAFS spectral characterization. *J. Mar. Syst.* **207**, 103344 (2020).

8. Shields, M. R., Bianchi, T. S., Gélinas, Y., Allison, M. A. & Twilley, R. R. Enhanced terrestrial carbon preservation promoted by reactive iron in deltaic sediments. *Geophys. Res. Lett.* **43**, 1149-1157 (2016).

9. Lalonde, K., Mucci, A., Ouellet, A. & Gélinas, Y. Preservation of organic matter in sediments promoted by iron. *Nature* **483**, 198-200 (2012).

10. Ma, W.-W., Zhu, M.-X., Yang, G.-P. & Li, T. Iron geochemistry and organic carbon preservation by iron (oxyhydr) oxides in surface sediments of the East China Sea and the south Yellow Sea. *J. Mar. Syst.* **178**, 62-74 (2018).

11. Salvadó, J. A. et al. Organic carbon remobilized from thawing permafrost is resequestered by reactive iron on the Eurasian Arctic Shelf. *Geophys. Res. Lett.* **42**, 8122-8130 (2015).

12. Wang, D., Zhu, M. X., Yang, G. P. & Ma, W. W. Reactive Iron and Iron‐Bound Organic Carbon in Surface Sediments of the River‐Dominated Bohai Sea (China) Versus the Southern Yellow Sea. *J. Geophys. Res. Biogeosci.* **124**, 79-98 (2019).

13. Tao, J., Ma, W., Li, W., Li, T. & Zhu, M. Organic carbon preservation by reactive iron oxides in South Yellow Sea sediments. *Haiyang Xuebao* **39**, 16-24 (2017).

14. Faust, J. C. et al. Millennial scale persistence of organic carbon bound to iron in

929   Arctic marine sediments. *Nat. Commun.* **12**, 275 (2021).

930 15. Faust, J. C. et al. Does Arctic warming reduce preservation of organic matter in
931   Barents Sea sediments? *Philosophical Transactions of the Royal Society A:*
932   *Mathematical, Physical and Engineering Sciences* **378**, 20190364 (2020).

933 16. LaRowe, D. E. et al. Organic carbon and microbial activity in marine sediments
934   on a global scale throughout the Quaternary. *Geochim. Cosmochim. Acta* **286**,
935   227-247 (2020).

936 17. Hu, Y. et al. Pore fluid compositions and inferred fluid flow patterns at the
937   Haima cold seeps of the South China Sea. *Mar. Pet. Geol.* **103**, 29-40 (2019).

938 18. Waelbroeck, C. et al. Sea-level and deep water temperature changes derived
939   from benthic foraminifera isotopic records. *Quaternary Science Reviews* **21**,
940   295-305 (2002).

941 19. Müller, A. L., Kjeldsen, K. U., Rattei, T., Pester, M. & Loy, A. Phylogenetic and
942   environmental diversity of DsrAB-type dissimilatory (bi) sulfite reductases.
943   *ISME J.* **9**, 1152-1165 (2015).